

## Laser-Induced Electron Diffraction for Probing Rare Gas Atoms

Junliang Xu,<sup>1,2</sup> Cosmin I. Blaga,<sup>2</sup> Anthony D. DiChiara,<sup>2</sup> Emily Sistrunk,<sup>2</sup> Kaikai Zhang,<sup>2</sup> Zhangjin Chen,<sup>1,3</sup>  
Anh-Thu Le,<sup>1</sup> Toru Morishita,<sup>1</sup> C. D. Lin,<sup>1</sup> Pierre Agostini,<sup>2</sup> and Louis F. DiMauro<sup>2</sup>

<sup>1</sup>*J. R. Macdonald Laboratory, Physics Department, Kansas State University, Manhattan, Kansas 66506-2604, USA*

<sup>2</sup>*Department of Physics, The Ohio State University, Columbus, Ohio 43210, USA*

<sup>3</sup>*Department of Physics, College of Science, Shantou University, Guangdong 515063, People's Republic of China*

(Received 6 February 2012; published 5 December 2012)

Recently, using midinfrared laser-induced electron diffraction (LIED), snapshots of a vibrating diatomic molecule on a femtosecond time scale have been captured [C. I. Blaga *et al.*, *Nature (London)* **483**, 194 (2012)]. In this Letter, a comprehensive treatment for the atomic LIED response is reported, a critical step in generalizing this imaging method. Electron-ion differential cross sections (DCSs) of rare gas atoms are extracted from measured angular-resolved, high-energy electron momentum distributions generated by intense midinfrared lasers. Following strong-field ionization, the high-energy electrons result from elastic rescattering of a field-driven wave packet with the parent ion. For recollision energies  $\geq 100$  eV, the measured DCSs are indistinguishable for the neutral atoms and ions, illustrating the close collision nature of this interaction. The extracted DCSs are found to be independent of laser parameters, in agreement with theory. This study establishes the key ingredients for applying LIED to femtosecond molecular imaging.

DOI: [10.1103/PhysRevLett.109.233002](https://doi.org/10.1103/PhysRevLett.109.233002)

PACS numbers: 33.20.Xx, 33.60.+q, 34.80.Bm, 34.80.Qb

An atom exposed to an intense low-frequency laser pulse can tunnel ionize, releasing an electron. Born in the laser's oscillating field, the electron may be accelerated back to recollide with the parent ion [1,2], incurring various electron-ion collision processes, such as elastic and inelastic scattering, and photorecombination. The recollision event is the basis of the strong-field rescattering model, which describes phenomena such as high-energy above-threshold ionization (HATI), nonsequential ionization, and high-harmonic generation. The combined elements of elastic scattering occurring on an optical-cycle time scale, e.g., femtoseconds, inherent in this model has generated interest in exploiting this as an ultrafast structural probe [3], analogous to diffraction using electron beams [4,5]. The viability of this self-imaging technique, dubbed laser-induced electron diffraction (LIED), has been addressed by several theoretical [6–9] and experimental [10,11] studies. A key principle was established by the quantitative rescattering (QRS) theory [7]: the *field-free* large-angle electron-ion (*e*-ion) elastic differential cross section (DCS) can be retrieved from a measured HATI electron momentum distribution. However in order for LIED to become an effective ultrafast imaging method, it is necessary that the valence (outer-shell) electrons of the target, e.g., molecules, play no significant role in the elastic process since their rearrangement which induces structural dynamics, i.e., motion of nuclei, is *de facto* unknown, and thus their interaction with the recolliding electron cannot be characterized.

Underpinning the concept of imaging via LIED is the ability to produce high-energy core-penetrating *e*-ion recollisions. Previous studies [12–16] using 0.8  $\mu\text{m}$  laser pulses have demonstrated the capability of extracting

DCSs from atoms and molecules. However the recollision energies are around a few tens of eV, too small to resolve the atomic core positions necessary for molecular imaging (see Refs. [11,17]). In this Letter, we report high-resolution photoelectron momentum distributions of rare-gas atoms recorded at midinfrared (MIR) wavelengths ( $>1 \mu\text{m}$ ) which generate recollision energies approaching 300 eV. The experiment exploits the strong wavelength dependence of an intense laser-atom interaction to promote high-energy recollisions while establishing the conditions for strong-field ionization [18,19]. In this study, the simplicity of an atomic target and the high-energy recollisions allows a comprehensive experimental and theoretical investigation of the *e*-ion interaction at large scattering angles. We show that the interaction is dominated by the strong short-range atomic potential while the valence electrons remain transparent, a prerequisite for imaging. Consequently, the experimental laser parameters used herein are directly aimed at establishing the foundation of time-resolved LIED imaging. Here we show that (1) above 100 eV recollision energies the DCSs at large angles are nearly the same for neutral atoms and singly-charged ions, (2) the DCSs extracted using different laser intensities and wavelengths are nearly identical for a given returning electron energy and (3) the returning electron wave packet expressed in field units obeys a simple universal scaling law, displaying no target dependence.

Details about the experimental setup and midinfrared laser systems can be found elsewhere [19–23]. Photoelectron momentum spectra are recorded using two different field-free time-of-flight electron spectrometers equipped with multichannel plate (MCP) detectors. To ensure good momentum resolution, small pinholes are installed in front of

the MCP detectors, restricting the collection angle to  $\pm 1$  degrees.

According to the QRS theory, the detected photoelectron angular distributions  $D(p, \theta)$  can be factorized as:

$$D(p, \theta) = W(p_r) \sigma(p_r, \theta_r), \quad (1)$$

where  $W(p_r)$  and  $\sigma(p_r, \theta_r)$  are the momentum distribution of returning wave packet and the DCS for free electrons scattering off the target ion, and  $p$ ,  $p_r$ ,  $\theta$  and  $\theta_r$  are the detected momentum, rescattering momentum, detected angle and rescattering angle, respectively. Detected momentum  $p$  and rescattering momentum  $p_r$  are related (in atomic units) by  $\mathbf{p} = \mathbf{p}_r - \mathbf{A}_r$ , where the additional momentum  $\mathbf{A}_r$  is the vector potential at recollision. According to the rescattering model [1,2], electrons that return at a given  $p_r$  follow either a long trajectory or a short trajectory. In this study the analysis is restricted to recollision energies  $\leq 2.3U_p$  instead of the maximum classical energy of  $3.17U_p$ . Here  $U_p$  is the cycle-averaged quiver energy of a free electron oscillating in an electromagnetic field. For these return energies, the wave packet is dominated by contribution from long trajectories since these electrons originate near the peak of the field where the tunneling rate is largest. In the experimental DCS analysis at fixed  $p_r$ , a momentum bin,  $\Delta p_r \sim 0.05$  a.u., is used. Compared to previously reported experiments performed with  $0.8 \mu\text{m}$  fields [12–16] (Keldysh parameter  $\gamma = \sqrt{I_p/2U_p} \geq 1$ , where  $I_p$  is the ionization potential), the present work is deep in the tunneling regime ( $\gamma < 0.47$ ).

Figure 1(a) presents the relative DCSs extracted in the case of argon for different laser parameters (given in the caption) for 100 eV recollision energies. The figure shows that irrespective of the laser parameters, the extracted DCSs are nearly identical thus demonstrating the robustness of the LIED approach. In contrast to the monochromaticity of a

typical electron beam used in conventional collision experiments, the LIED returning wave packet is broadband, ranging from 0 to  $3.17U_p$ . Consequently, a series of DCSs for different returning energies can be extracted from a *single* measured photoelectron momentum distribution. Figures 1(b) and 1(c) depict two additional LIED DCSs at 150 eV and 200 eV energies, respectively, extracted from experimental data taken at  $235 \text{ TW}/\text{cm}^2$  for  $2.0 \mu\text{m}$  pulses. A general feature of intense laser-atom interaction at longer wavelength is a “squeezing” of the angular distribution of direct electrons along the laser polarization direction compared to shorter wavelengths; consequently, contamination of the DCSs with direct electrons is minimized and confined to small angles. Figure 1 shows that the DCSs derived using  $2.0 \mu\text{m}$  pulses are extracted from  $30^\circ$  to  $180^\circ$  scattering angles, compared to the smaller  $110^\circ$ – $180^\circ$  range reported in  $0.8 \mu\text{m}$  experiments [12,13]. Thus, MIR lasers provide large-range momentum transfer, a critical requirement for achieving good spatial resolutions for molecular imaging.

The extracted DCS at each energy is also compared to theoretical calculations for field-free  $e$ -Ar<sup>+</sup> collisions. The  $e$ -Ar<sup>+</sup> interaction is approximated by a model potential in the form

$$V(r) = -(1 + a_1 e^{-a_2 r} + a_3 r e^{-a_4 r} + a_5 e^{-a_6 r})/r, \quad (2)$$

where the parameters in the potential are given in Ref. [24]. These parameters are obtained by fitting to the binding energies of the ground state and first few excited states of Ar, with the constraint that  $1 + a_1 + a_5 = Z$ , where  $Z$  represents the nuclear charge. The calculated DCSs depicted in Fig. 1 are in good agreement with the measurement. Each graph also shows the experimental DCS from  $e$ -Ar collisions [25]. The neutral and ionic DCSs for return energies above 100 eV are essentially identical.

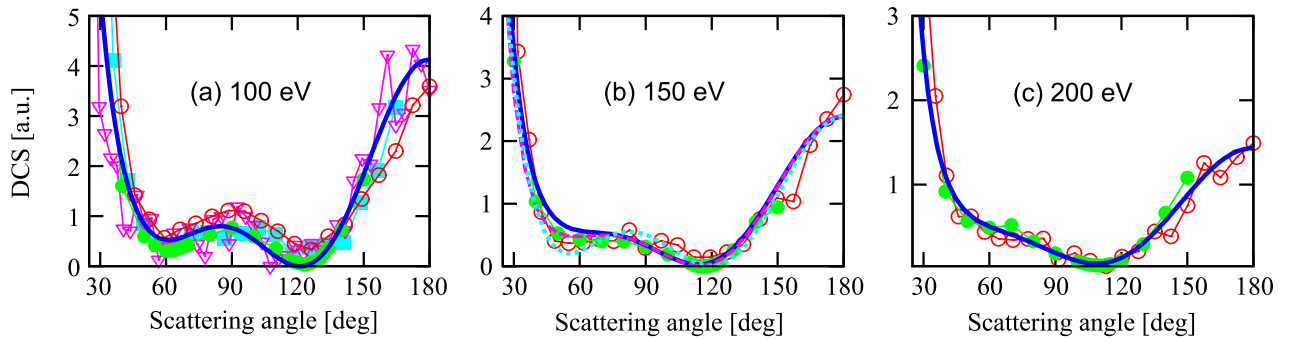


FIG. 1 (color online). (a) Extracted DCSs of Ar at 100 eV from HATI spectra for different combinations of laser intensities and wavelengths. Red empty circles:  $2 \mu\text{m}$  and  $235 \text{ TW}/\text{cm}^2$ ; magenta triangles:  $2 \mu\text{m}$  and  $200 \text{ TW}/\text{cm}^2$ ; cyan solid squares:  $2.3 \mu\text{m}$  and  $380 \text{ TW}/\text{cm}^2$ . The corresponding  $U_p$  are 88 eV, 75 eV and 188 eV, respectively. Green filled circles are experimental DCSs for the  $e$ -Ar collision using electron guns [25], and the blue full curve are theoretical  $e$ -Ar<sup>+</sup> DCSs. (b) At 150 eV,  $e$ -Ar<sup>+</sup> DCS (red empty circles) is extracted from HATI spectra at  $2 \mu\text{m}$  and  $235 \text{ TW}/\text{cm}^2$ , in comparison to the theoretical  $e$ -Ar<sup>+</sup> DCS (blue solid line) and experimental  $e$ -Ar DCS (green filled circles) [25]. (c) Same as (b) but for 200 eV. In (b), the theoretical DCS for an  $e$ -neutral collision [30] at 150 eV is also depicted by the magenta dashed line, in comparison to both the experimental and theoretical  $e$ -ion DCSs. The cyan dotted line in (b) is the DCS calculated using the atomic potential retrieved from an experimental  $e$ -ion DCS at 150 eV, see text.

All the extracted LIED DCS data faithfully reproduce the evolution in the shape seen in the  $e$ -neutral measurements and  $e$ -ion calculations as a function of electron energy. For example, as the energy increases the diffracted peak at  $180^\circ$  is suppressed compared to the low-angle signal, whereas the maximum at about  $90^\circ$  becomes less conspicuous and flattens at 200 eV. The similarity of the  $e$ -ion and  $e$ -neutral DCSs demonstrates that the long-range Coulomb potential plays little role in large angle scattering. In other words, scattering occurs close to the atomic center (less than  $0.5 \text{ \AA}$  for Ar at 100 eV), where the neutral and ionic potentials are essentially identical.

Figure 2 shows the DCSs extracted from the HATI distribution of (a) Kr at 150 eV and (b) Xe at 50 eV, in comparison to Ar data in Fig. 1. These two atoms are irradiated with 50 fs,  $2 \mu\text{m}$  pulses at  $180 \text{ TW/cm}^2$  and  $72 \text{ TW/cm}^2$ , respectively. Each figure also plots the experimental  $e$ -neutral DCS [26,27]. Over the common angular region the two measured DCSs agree well except that the LIED values show larger scattering. Two theoretical curves are also shown in each figure, one (solid curve) from the simple model potential approach for  $e$ -cation collisions described above while the other (dashed curve) is based on a more sophisticated  $e$ -neutral atom collision model described in the literature [28,29]. Just to compare with Kr at 150 eV, Fig. 1(b) also depicts a theoretical  $e$ -neutral atom collision DCS of Ar at the same energy [30]. For Ar and Kr, the difference between the two theories is small

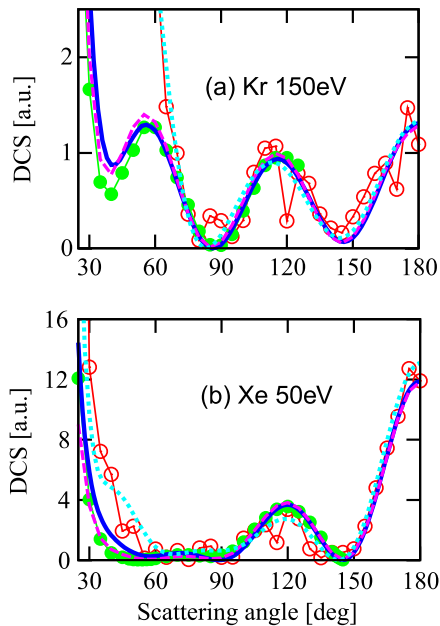


FIG. 2 (color online). Comparison of DCSs from LIED for Kr and Xe at 150 and 50 eV, respectively. DCS from HATI: red empty circles; theoretical  $e$ -ion: blue solid lines; experimental  $e$ -neutral: green filled circles [26,27]; theoretical  $e$ -neutral: magenta dashed lines. DCSs calculated from these fitted potentials are also shown by the cyan dotted lines.

over a broad angular range from  $70^\circ$  to  $180^\circ$ . For Xe, due to the lower scattering energy, the two theories overlap at angles  $>110^\circ$  but show significant deviation at smaller angles (see the Supplemental Material [31] for a clearer comparison on a logarithmic scale). Based on the evidence shown in Figs. 1 and 2, one can conclude that the  $e$ -neutral and  $e$ -cation DCSs are the same for collision energies above 100 eV and the scattering angle range shown. This observation validates the LIED approach for structural analysis using large angle scattering at collision energies  $\geq 100 \text{ eV}$ .

An effective means for confirming the sensitivity of our results mainly to the short range part of the potential is provided by comparing known potentials and those retrieved from the measured DCS via a genetic algorithm (GA) fitting procedure [32,33]. Using Eq. (2) and the data in Fig. 1(b) and 2, the 6 parameters can be extracted from the experimentally determined large angle scattering between  $[70^\circ, 180^\circ]$ . To be fair, the condition  $1 + a_1 + a_5 = Z$  is not assumed, i.e., no knowledge of the atom's nuclear charge. To assist the GA's convergence to a physically meaningful solution, we impose constraints on effective nuclear charge  $Z(r)$ , defined as  $-rV(r)$ , that  $Z(r) > 0$ ,  $Z$  is between 0 and 70, and  $dZ(r)/dr < 0$ . These are clearly satisfied for the atomic potentials of interest here. The best fit for each model potential retrieves nuclear charges  $Z$  of 18.6 for Ar, 38.7 for Kr and 50.0 for Xe, which are close to the actual values. The accuracy is not sufficient to uniquely determine the atomic species but adequate for differentiating the rare gas atom. This is not a limitation of LIED but instead a constraint imposed by retrieving the potential from DCSs at a certain range of collision energy, i.e., only a specific region is probed by the scattering experiment. This can be seen by comparing the retrieved effective charges (dotted line) with those fitted (solid line) in Ref. [24], as illustrated in Fig. 3. Note that for Ar and Kr, the two curves agree out to a distance of 0.5 a.u. The discrepancy at larger  $r$  is not surprising since this part of the potential is not important for the DCSs at 150 eV and scattering angles above  $38^\circ$  for Ar and  $60^\circ$  for Kr. This exemplifies an important but obvious lesson in scattering

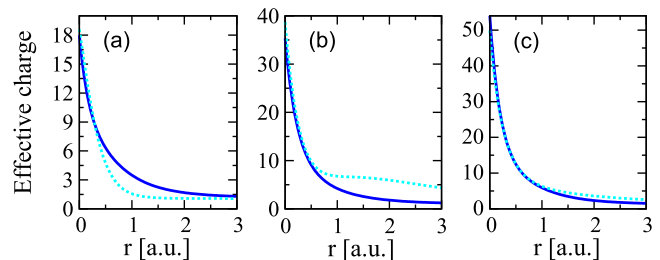


FIG. 3 (color online). Retrieved atomic potentials with DCS from the LIED data in Fig. 1(b) and 2 for (a) Ar, (b) Kr, and (c) Xe, respectively. Cyan dotted lines are the fitted effective charges as a function of  $r$ , compared to a “known” potential for each atom (blue solid lines).

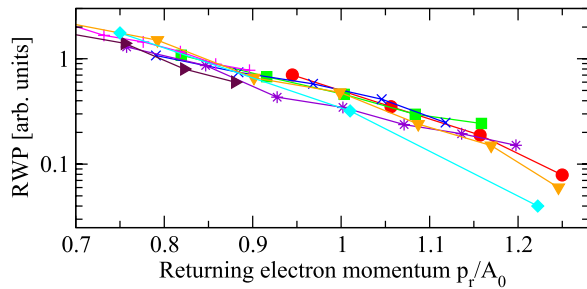


FIG. 4 (color online). Returning electron wave packets against returning electron momentum extracted from the photoelectron spectra for different laser parameters and different atoms. (Target, wavelength in  $\mu\text{m}$ , intensity in  $\text{TW}/\text{cm}^2$ ) are: red filled circles: (Ar, 1.7, 208); green solid squares: (Ar, 2.0, 200); blue crosses: (Ar, 2.0, 215); purple asterisks: (Ar, 2.0, 235); magenta pluses: (Ar, 2.3, 380); orange solid inverted triangles: (Kr, 2.0, 180); maroon solid right triangles: (Kr, 2.3, 98); cyan solid diamonds: (Xe, 2.0, 72).

theory that each event probes only a certain aspect of the target. As a further illustration, the retrieved potential from the GA method is used to calculate the DCSs [cyan dotted lines in Fig. 1(b) and 2]. It shows that the DCS extracted from the HATI measurements are indeed well reproduced, despite that the difference in the two potentials at larger  $r$ .

One additional comment, the relatively low return energy of 50 eV for the Xe case shown in Fig. 3(c) results in a more effective probe at large  $r$ , thus producing better agreement between the potentials up to 1 a.u. However at low energy, electron exchange and many-body effects become increasingly important, rendering an effective potential description of a collision process as increasingly inaccurate. Thus one often does not attempt to retrieve the target “structure” from the measured cross sections at low energies.

According to Eq. (1), the spectral weight of the returning wave packet (RWP) can be extracted from the measured angular distribution assuming knowledge of the absolute DCS. The experimental RWP at fixed  $p_r$  is defined as the overall normalization factor that multiplies the absolute DCS. Scanning  $p_r$ , one obtains the RWP as a function of returning electron momentum. Figure 4 shows the extracted experimental returning wave packets for the first time for Ar, Kr, and Xe at different laser parameters. The monotonic decrease in the returning wave packet spectral density with increasing electron momentum is a universal feature observed in all collected data sets. Plotting the electron momentum in units that correspond to the maximum value of the vector potential  $A_0$ , a scaling law  $W(p_r/A_0) \sim (p_r/A_0)^{-2.6 \pm 0.3}$  is found. The target independence of the RWP is consistent with the assumptions of the QRS theory. The RWP shown in Fig. 3 includes the experimental averaging over the focal volume, thus filtering out the oscillatory structure seen in the single-intensity calculations (see Fig. 14 in Ref. [7]). Similar results were shown earlier by Levesque *et al.* [34] for high harmonic

generation. Interestingly, given the broadband nature of the returning electron wave packet, one can view LIED as a series of conventional electron diffraction experiments repeated at different collision energies. Thus, LIED records a two-dimensional (2D) elastic DCS map, which, in principle, allows more accurate retrieval of the target structure since the fit is over the entire 2D map as opposed to a single DCS curve.

In conclusion, we have demonstrated that at midinfrared wavelengths, laser-induced electron diffraction is a powerful method to extract accurate  $e$ -ion collision DCSs with dynamic ranges comparable with traditional gas-phase electron diffraction methods. The measured electrons at long wavelengths promote hard collisions with the atomic core and thus the DCS for the atomic cation is the same as that for the neutral. This is a necessity for dynamic molecular imaging, as it signifies that the  $e$ -molecule interaction will be dominated by a well-localized, strong short-range *atomic-like* potential while the delocalized, valence electrons are transparent, which also holds good promise for achieving suitable spatial resolutions using LIED. The experimental results provide further verification of the QRS theory prediction that the extracted DCS does not depend on the laser parameters, and that the returning electron wave packet plotted in units of the maximum vector potential is independent of the target and the laser intensity. These results provide essential ingredients needed for deploying LIED for investigating more complex molecules and time-resolved structure retrieval of a molecule under conformal transformation, as demonstrated in revealing the bond relaxation of  $\text{O}_2$  and  $\text{N}_2$  molecules following tunneling ionization [20].

This work was performed with support from US DOE under DE-FG02-06ER15832 at Kansas State University and the NSF under Grant No. PHY-1004778 at Ohio State University. L.F.D. acknowledges support from the Hagenlocker chair. Z.C. acknowledges support by STU Scientific Research Foundation for Talents.

- 
- [1] K. J. Schafer, B. Yang, L. F. DiMauro, and K. C. Kulander, *Phys. Rev. Lett.* **70**, 1599 (1993).
  - [2] P. B. Corkum, *Phys. Rev. Lett.* **71**, 1994 (1993).
  - [3] T. Zuo, A. D. Bandrauk, and P. B. Corkum, *Chem. Phys. Lett.* **259**, 313 (1996).
  - [4] *Stereochemical Applications of Gas-Phase Electron Diffraction*, edited by I. Hargittai and M. Hargittai (VCH, New York, 2009) and references therein.
  - [5] A. H. Zewail and J. M. Thomas, *4D Electron Microscopy: Imaging in Space and Time* (Imperial College Press, London, 2010).
  - [6] T. Morishita, A.-T. Le, Z. Chen, and C. D. Lin, *Phys. Rev. Lett.* **100**, 013903 (2008).
  - [7] Z. Chen, A.-T. Le, T. Morishita, and C. D. Lin, *Phys. Rev. A* **79**, 033409 (2009).

- [8] A. Čerkić, E. Hasović, D.B. Milošević, and W. Becker, *Phys. Rev. A* **79**, 033413 (2009).
- [9] M. V. Frolov, N. L. Manakov, and A. F. Starace, *Phys. Rev. A* **79**, 033406 (2009).
- [10] M. Meckel *et al.*, *Science* **320**, 1478 (2008).
- [11] S. K. Lee, Y. F. Lin, L. Yan, and W. Li, *J. Chem. Phys.* **116**, 1950 (2012).
- [12] D. Ray *et al.*, *Phys. Rev. Lett.* **100**, 143002 (2008).
- [13] M. Okunishi, T. Morishita, G. Prümper, K. Shimada, C. D. Lin, S. Watanabe, and K. Ueda, *Phys. Rev. Lett.* **100**, 143001 (2008).
- [14] M. Okunishi, H. Niikura, R. R. Lucchese, T. Morishita, and K. Ueda, *Phys. Rev. Lett.* **106**, 063001 (2011).
- [15] C. Cornaggia, *J. Phys. B* **42**, 161002 (2009).
- [16] A. Gazibegović-Busuladžić *et al.*, *Phys. Rev. A* **84**, 043426 (2011).
- [17] J. Xu, Z. Chen, A.-T. Le, and C. D. Lin, *Phys. Rev. A* **82**, 033403 (2010).
- [18] J. Tate, T. Auguste, H. G. Muller, P. Salières, P. Agostini, and L. F. DiMauro, *Phys. Rev. Lett.* **98**, 013901 (2007).
- [19] P. Colosimo *et al.*, *Nat. Phys.* **4**, 386 (2008).
- [20] C. I. Blaga, J. Xu, A. D. DiChiara, E. Sistrunk, K. Zhang, P. Agostini, T. A. Miller, L. F. DiMauro, and C. D. Lin, *Nature (London)* **483**, 194 (2012).
- [21] A. D. DiChiara, E. Sistrunk, T. A. Miller, P. Agostini, and L. F. DiMauro, *Opt. Express* **17**, 20959 (2009).
- [22] C. P. Hauri *et al.*, *Opt. Lett.* **32**, 868 (2007).
- [23] C. I. Blaga, F. Catoire, P. Colosimo, G. G. Paulus, H. G. Muller, P. Agostini, and L. F. DiMauro, *Nat. Phys.* **5**, 335 (2009).
- [24] X. M. Tong and C. D. Lin, *J. Phys. B* **38**, 2593 (2005).
- [25] J. F. Williams and B. A. Willis, *J. Phys. B* **8**, 1670 (1975).
- [26] A. Danjo, *J. Phys. B* **21**, 3759 (1988).
- [27] D. F. Register, L. Vuskovic, and S. Trajmar, *J. Phys. B* **19**, 1685 (1986).
- [28] J. E. Sienkiewicz and W. E. Baylis, *J. Phys. B* **25**, 2081 (1992).
- [29] R. P. McEachran and A. D. Stauffer, *J. Phys. B* **17**, 2507 (1984).
- [30] S. N. Nahar and J. M. Wadehra, *Phys. Rev. A* **35**, 2051 (1987).
- [31] See Supplemental Material at <http://link.aps.org/supplemental/10.1103/PhysRevLett.109.233002> for (i) detailed comparison on  $e$ -neutral-atom and  $e$ -ion scattering cross sections on logarithmic scale, (ii) the genetic algorithm fitting procedure, and (iii) theoretical calculations of  $e$ -ion scattering DCS.
- [32] D. L. Carroll, “FORTRAN genetic algorithm driver”, 1999, <http://cuaerospace.com/carroll/ga.html> (accessed in May 2008).
- [33] J. Xu, H.-L. Zhou, Z. Chen, and C. D. Lin, *Phys. Rev. A* **79**, 052508 (2009).
- [34] J. Levesque, D. Zeidler, J. P. Marangos, P. B. Corkum, and D. M. Villeneuve, *Phys. Rev. Lett.* **98**, 183903 (2007).